LASER & PHOTONICS REVIEWS

www.lpr-journal.org

Full Complex-Amplitude Modulation of Second Harmonic Generation with Nonlinear Metasurfaces

Zelin Hao, Wenwei Liu, Zhancheng Li, Zhi Li, Guangzhou Geng, Yanchun Wang, Hua Cheng, Hammad Ahmed, Xianzhong Chen, Junjie Li, Jianguo Tian,* and Shuqi Chen**

Metasurfaces have shown unprecedented capabilities and flexibilities for optical wave manipulation, which provide a powerful platform for the integration and minimization of multifunctional optical devices. However, the realization of the multidimensional manipulation of harmonic waves generated by nonlinear metasurfaces is still a challenge due to the lack of a theoretical guidance. Here, an efficient design strategy of nonlinear metasurfaces based on the hydrodynamic model of the free electron dynamics is demonstrated to realize the full complex-amplitude modulation of the second harmonic generation (SHG). As a proof concept, three multifunctional nonlinear metasurfaces are designed, in which both the amplitude and the phase of the SHG waves are efficiently and independently manipulated. With numerical and experimental validations, the proposed nonlinear metasurfaces can realize the spin-selective SHG optical vortices with independent topological charges. The design strategy of nonlinear metasurfaces shall boost the applications of nonlinear metasurfaces in optical information, optical multifunctional integration, and so on.

1. Introduction

Recently, flat integrated optical devices have been considered as one of the most challenging and promising research fields. There is an ever-increasing demand for new approaches to realizing the effective manipulation of optical waves. Metasurfaces, the 2D artificial arrays of nanoparticles, have shown unprecedented capabilities and provide a compact platform for manipulating optical waves at the subwavelength scale.[1–7] Benefiting from the strong light–matter interactions within nanostructures, a series of metasurfaces have been proposed for novel applications, such as spin–orbit interaction,[8–10] light focusing and imaging,[11–13] anomalous refraction and reflection,[14–16] optical spin Hall effect,[17,18] and asymmetric transmission.[19,20] Phase-modulated metasurfaces, consisting of the Pancharatnam–Berry (P–B) phase elements, have shown prominent advantages in phase manipulation engineering.[21,22] Compared with the phase-only manipulation,[23–25] the complex-amplitude (phase and amplitude) modulation of optical waves with metasurface can significantly improve the performance of the optical devices, including the realization of the energy distribution of the multichannels and the improvement of the transmission accuracy of the optical signals.[26–29] For example, Liu et al. realized a multifunctional metasurface to tailor the intensity of each information channel without intrinsic noises compared with phase-/intensity-only devices in linear photonics.[30] However, complex-amplitude modulation of the high harmonic generation still remains a challenge.

The latest advances in metasurfaces revealed their great advantages for nonlinear wave generation and manipulation.[31–50]

Z. Hao, W. Liu, Z. Li, Z. Li, G. Geng, Y. Wang, H. Cheng, J. Tian, S. Chen
The Key Laboratory of Weak Light Nonlinear Photonics
Ministry of Education
Renewable Energy Conversion and Storage Center
School of Physics and TEDA Institute of Applied Physics
Nankai University
Tianjin 300071, China
E-mail: hcheng@nankai.edu.cn; jjtian@nankai.edu.cn; schen@nankai.edu.cn

H. Ahmed, X. Chen
Institute of Photonics and Quantum Sciences
School of Engineering and Physical Sciences
Heriot-Watt University
Edinburgh EH14 4AS, UK

J. Li
Beijing National Laboratory for Condensed Matter Physics
Institute of Physics
Chinese Academy of Sciences
Beijing 100190, China

S. Chen
The Collaborative Innovation Center of Extreme Optics
Shanxi University
Taiyuan, Shanxi 030006, China

S. Chen
Collaborative Innovation Center of Light Manipulations and Applications
Shandong Normal University
Jinan 250358, China

DOI: 10.1002/lpor.202100207

The phase-matching condition in nonlinear process can be significantly relaxed in metasurfaces since their thickness is at the subwavelength scale. Meanwhile, the localized surface plasmonic resonances in metasurfaces can generate strong enhancement of the electromagnetic fields near the nanoparticles and can greatly boost the efficiency of high harmonic generation. Nonlinear metasurfaces have been used widely in many applications, such as giant enhancement of harmonic generation,[31–35] nonlinear metalens,[36–38] nonlinear optical holography,[39–41] nonlinear vortex beams,[42,43] and nonlinear information coding.[44,45] Nonlinear phase-modulated metasurfaces have been used to realize complete control over the propagation of the high harmonic generation.[46–50] However, previous nonlinear phase-modulated metasurfaces suffer from intrinsic noises due to the loss of intensity information, and such phase-only metasurfaces also cannot realize intensity-only applications such as resolution test targets. Simultaneous manipulation of amplitude and phase of the nonlinear optical signals based on metasurface, which is eagerly anticipated by the scientific community, has not been well explored yet.

Here, we propose a design principle of nonlinear metasurfaces to realize the full complex-amplitude modulation of the second harmonic generation (SHG). Based on the hydrodynamic model of the free electron dynamics, the proposed nonlinear metasurfaces can simultaneously manipulate the amplitude and the phase of SHG. In order to confirm the validity of our theory, we designed a nonlinear plasmonic metasurface that can generate four second harmonic optical vortices with independent topological charges. The designed metasurface consists of gold nanoparticles with threefold rotational symmetry of different sizes. We investigate the SHG process of the nanoparticles and perform full-wave nonlinear simulation using the hydrodynamic model. Different from traditional phase-modulated metasurface, we employ amplitude and phase manipulating simultaneously by encoding the information into the geometry and the spatial orientation of the nanoparticles. Furthermore, the spin-selective characteristic of the designed metasurface has been experimentally demonstrated. The designed metasurface breaks the conjugate symmetry of nonlinear phase-modulated phase for right-handed circularly polarized (RCP) and left-handed circularly polarized (LCP) incident light. Besides, we design the spin-controlled interleaved nonlinear metasurface that can generate different series of multichannel vortex beams when illuminated by different circularly polarized light.

2. Results and Discussion

The key point to realize simultaneous manipulation of the amplitude and the phase of second harmonic (SH) waves is to predict the nonlinear properties of the plasmonic nonlinear metasurfaces. In order to analyze the second-order nonlinear properties of the nanoparticles, we studied the nonlinear radiation from the nanoparticle by employing the hydrodynamic model of the free electron dynamics. We incorporated the hydrodynamic model into a finite element numerical simulation method to obtain the far-field nonlinear radiation of the designed nanoparticle. By utilizing the hydrodynamic model, we can calculate the nonlinear surface current distribution which can be expressed by the fundamental polarization. The effective nonlinear current density $\mathbf{K}_{\mathrm{NL}}$ at the surface of a nanoparticle can be expressed as[51]

$$\mathbf{K}_{\mathrm{NL}} = 2i\omega \int_{\xi=0}^{\xi=l} \mathbf{P}_2^S(\mathbf{r})\,\mathrm{d}\mathbf{r} \tag{1}$$

where $\mathbf{P}_2^S$ represents the nonlinear surface polarization and can be obtained by

$$\mathbf{P}_2^S = -\frac{1}{2n_0 e}\left[(\nabla\cdot\mathbf{P}_1)\,\mathbf{P}_1 + \frac{\omega}{2\omega+i\gamma}(\mathbf{P}_1\cdot\nabla)\,\mathbf{P}_1\right] \tag{2}$$

where $\mathbf{P}_1$ represents the fundamental polarization, n_0 is the charge density, and γ is electron collision rate. Then, the x- and y-components of the nonlinear current at the upper and lower surfaces of the nanoparticle can be simplified as

$$K_x = \frac{i\omega}{n_0 e}\Delta P_z P_x \tag{3}$$

$$K_y = \frac{i\omega}{n_0 e}\Delta P_z P_y \tag{4}$$

where ΔP_z represents the difference of the z-component of the polarization at the surface of the nanoparticle. Because the z-component of the nonlinear current makes a negligible contribution to the far-field SH radiation, we simplified our simulation model by neglecting the z-component of the nonlinear current in the following nonlinear simulation. The nonlinear surface currents of all surfaces of the designed nanoparticle are used as the excitation source to achieve the simulation of the SH radiation. Therefore, the amplitude and the phase of the SH radiation can be quantitatively calculated and the complex-amplitude modulation of the SH waves can be further realized by varying the size and the orientation of the designed nanoparticles.

The designed nonlinear metasurface consists of gold nanoparticles with threefold (C_3) rotational symmetry. According to the selection rules, the C_3-symmetric nanoparticles allow only the generation of the cross-polarized SHG.[52,53] **Figure 1**a shows the schematic of the designed C_3-symmetric gold nanoparticle on the SiO_2 substrate. The C_3-symmetric nanoparticles are located at the centers of the hexagonal unit cell. The side length of the hexagon silica substrate P is $200\sqrt{3}$ nm and the period of nanoparticles is 600 nm. The nanoparticle is characterized by the arm length l, the arm width w, and the height h. We designed and fabricated the multiplexing metasurface consisting of the designed C_3-symmetric gold nanoparticles. The simulated (red line) and the measured (blue line) linear transmission spectra under RCP illumination are displayed in Figure 1b. The simulated result was performed by using the commercially available software COMSOL Multiphysics based on the finite element method. The permittivity of gold and the SiO_2 substrate was taken from Palik's handbook.[54] A trough with simulated transmittance lower than 0.2 can be observed at 1550 nm, which is attributed to the excitation of the plasmonic electric dipole within the nanoparticle. In the experiments, the electric dipole mode can be observed at 1588 nm, which is slightly redshifted compared with the simulated result.

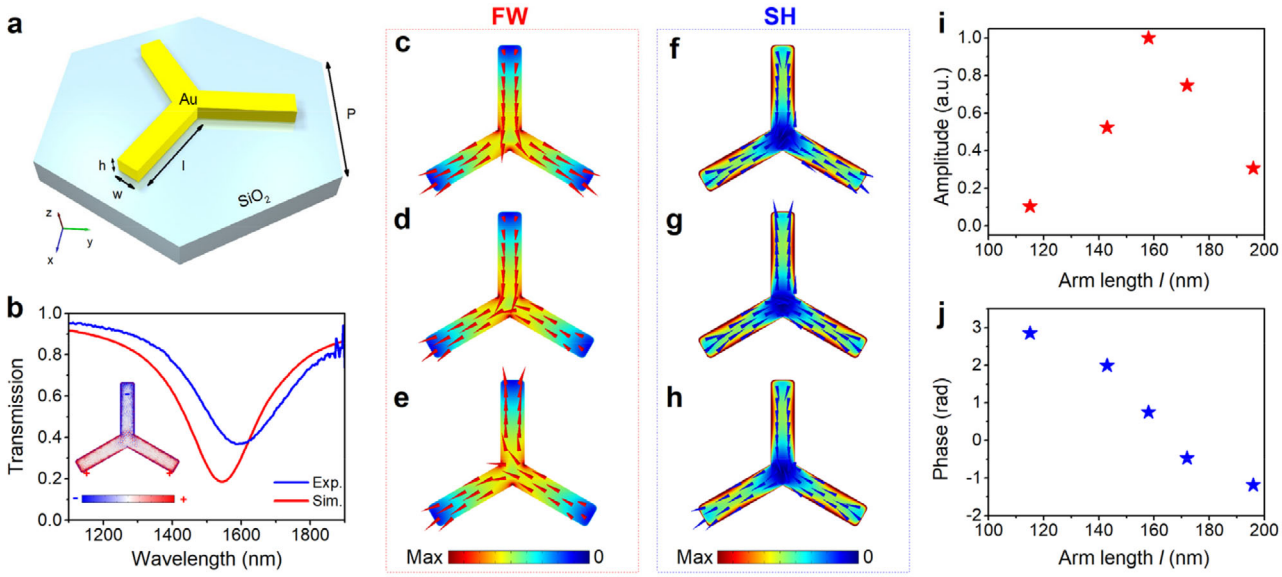

Figure 1. Illustration of the designed C_3-symmetric gold nanoparticle for simultaneous manipulation of the amplitude and the phase of the SH waves. a) Schematic of the designed nanoparticle. The unit cell of the proposed metasurface consists of a gold nanoparticle with threefold rotational symmetry and a regular hexagon silica substrate. The arm length *l*, the arm width *w*, and the height of *h* of the nanoparticle are 158, 45, and 30 nm, respectively. b) Simulated (red lines) and measured (blue lines) transmission spectra of the proposed metasurface under RCP illumination. The inset shows the charge distribution of the C_3-symmetric nanoparticle at the wavelength of 1550 nm. c–e) Three different snapshots of the current flows (red arrows) and the density distribution (color map) of the fundamental polarization at the upper surface of the C_3-symmetric nanoparticle. f–h) The current flows (blue arrows) and the density distribution (color map) of the SH currents at the upper surface of the C_3 nanoparticle snapshotted at three corresponding times. Variation of i) the amplitude and j) the phase of the outgoing SH waves with the changing of the structural parameter *l* of the designed nanoparticles, in which *l* is equal to 115, 196, 143, 172, and 158 nm, respectively.

Figure 1c–e shows the fundamental polarization distribution on the upper surface of the designed nanoparticle for RCP incidence at the operating wavelength of 1550 nm. By utilizing the hydrodynamic model, we calculated the nonlinear surface currents in all surfaces and achieved a complete description of the SHG process in the designed nanoparticle. The surface currents for the SH waves at the upper surface of the nanoparticle are displayed in Figure 1f–h. The fundamental polarization shows different distributions at three different moments. At the corresponding moments, we observed that the flow of the nonlinear surface currents changed periodically. Three nonlinear surface current distribution diagrams show the variation tendency in a complete period, while the fundamental polarization distributions only show variation tendency in half a period. Different from the SH current distributions in the split ring resonators,[55] the surface currents in the designed nanoparticles do not have a uniform directivity. The calculated SH radiation is determined by the nonlinear current distributions in the whole period. The nonlinear surface current density at the edge of the designed nanoparticle is much stronger than that within the structure. Therefore, the nonlinear surface currents at the edge play an important role in the far-field SH radiation. For our designed nanoparticles, the nonlinear currents in the upper and the lower surfaces contribute more to the far-field radiation than the side surfaces. The simulated electric field distribution of the SH waves (see Figure S1 in the Supporting Information) shows that only the SH waves with the opposite spin angular momentum can radiate to the far field. The spin-selective characteristic of the designed nanoparticle can confirm the selection rules for the harmonic generation of the circular polarized fundamental waves (FWs): for circular-polarized (σ) FWs propagating along the rotational axis of the C_3-symmetric nanoparticle, only SHG with opposite optical spin ($-\sigma$) can be generated. To make a further validation, we analyzed the nonlinear optical responses of the designed C_3-symmetric nanoparticle by calculating the wavelength-dependent SHG intensities under the pumping of the LCP and RCP FWs from 1400 to 1700 nm (see Figure S2 in the Supporting Information). The maximum SHG intensity is observed at the FW of 1530 nm, which is close to the resonance wavelength in Figure 1b. The SHG intensity decreases as the wavelength of the FW shifts from 1530 nm. Meanwhile, the results verify that the intensities of the SHG waves with opposite optical spin to that of the FWs are much stronger, which further validates the selection rules for the harmonic generations.

To achieve complete control over the amplitude and phase of the SH waves, we calculated the SH radiation for a set of C_3-symmetric nanoparticles under RCP illumination. The arm width of the simulated C_3-symmetric nanoparticle was fixed at 45 nm, while the amplitude modulation is realized by changing the arm length. Considering the experimental feasibility, the normalized amplitude is divided into five states, which are 0.103, 0.306, 0.524, 0.748, and 1, respectively. Five nanoparticles were optimized to obtain the five-level amplitude modulation (Figure 1i). The phase of the scattered SH waves for our designed nanoparticles is shown in Figure 1j. Note that the results in Figure 1i,j remain unchanged for LCP illumination since the nanoparticles are in C_3 rotational symmetry. The phase manipulation of the SH waves can be realized by involving both the resonant phase ψ and the geometry phase $3\sigma\theta$, and the phase

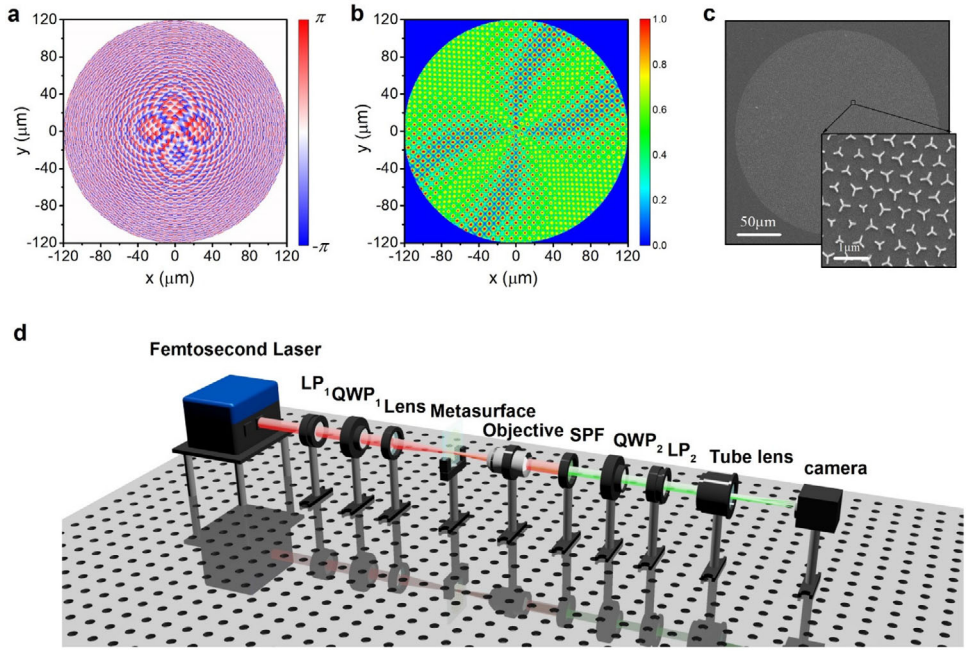

Figure 2. Design details of the OAM multiplexing metasurface and the experimental setup. a) Calculated phase profile for focusing multichannel vortex beams. b) Five-level amplitude profile for focusing multichannel vortex beams. c) Scanning electron microscopy (SEM) images of the fabricated metasurface. The inset zooms in the designed metasurface. d) Schematic of the measurement setup. The RCP light can be generated by a polarizer (LP_1) and a quarter-wave plate (QWP_1). Another set of a QWP_2 and a LP_2 is used to measure the signal with opposite circular polarization. The SH signals are collected by a tube lens and a scientific camera.

of the SH waves can be expressed as $\Phi = \psi + 3\sigma\theta$. It is worth mentioning that, although the nonlinear resonant phase in our designed nanoparticles is discrete, we can continuously control the phase of the SH waves by varying the orientation angle θ of the designed nanoparticle. The further analysis proved that the phase of the SH waves varies proportionally with the rotation angle of the nanoparticle, while the amplitude of the SH waves is not affected by the rotation angle of the nanoparticle (see Figure S3 in the Supporting Information). Therefore, the full complex-amplitude modulation of the SH waves can be realized by varying the size and the orientation of the designed nanoparticles.

To experimentally verify our theory, we designed and fabricated the orbital angular momentum (OAM) multiplexing metasurfaces that could generate multichannel vortex beams. The off-axis design is utilized to realize both the focusing of the multichannel vortex beams for enhancing the weak SHG signals, and the control over the position of the focal spots in the free space. Thus, the metasurfaces need to incorporate the phase profile of off-axis focusing and the vortex plate terms

$$\Phi(r,\varphi) = \frac{2\pi}{\lambda}\left(\sqrt{f^2 + r^2 - 2rf\sin\theta\cos(\varphi_f - \varphi)} - f\right) + l\varphi \quad (5)$$

where $f = 300$ μm is the focal length, and $\theta = 4.76°$ is the off-axis angle. The parameter φ_f stands for the azimuth of the focus position and l represents the topological charge. By superimposing the complex electric fields of the OAM beam channels in the metasurface plane, we can calculate the complex electric fields of the designed metasurface. The amplitude and the phase can be acquired and expressed as

$$A = \text{abs}\left(\sum_{k=1}^{n} a_k \exp(i\Phi_k)\right) \quad (6)$$

$$\phi = \arg\left(\sum_{k=1}^{n} a_k \exp(i\Phi_k)\right) \quad (7)$$

where a_k is the amplitude scale factor of the different OAM beams and we defined $a_k = 1$. We designed four off-axis optical vortices at the focal plane and the topological charges were different from each other. The calculated phase and amplitude profiles of the electric field in the metasurface plane are illustrated in **Figure 2**a,b, respectively. The metasurfaces were fabricated by standard electron-beam lithography (EBL) and lift-off process. Figure 2c shows the scanning electron microscopy (SEM) image of the designed metasurface, in which the multichannel information is encoded to the size and the rotation angle of the nanoparticles. In the experimental setup, the nonlinear optical vortices signal can be detected by the measurement system, which is shown in Figure 2d.

As shown in **Figure 3**a, we designed the first sample with four channels under RCP illumination and set the focusing optical vortices F_1, F_2, F_3, and F_4 with topological charges $l_1 = +1$, $l_2 = +3$, $l_3 = +2$, and $l_4 = -2$, respectively. We numerically calculated the

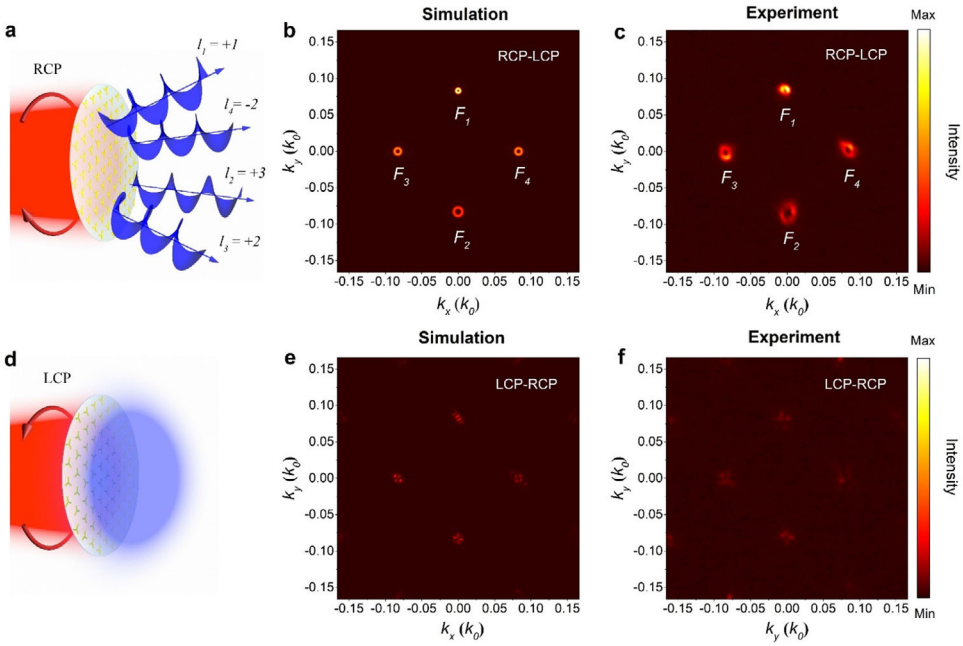

Figure 3. Spin-selective generations of four SH optical vortices with independent topological charges by the designed nonlinear metasurfaces. a) Schematic of the multichannel vortex beams generated with the designed metasurface under RCP illumination. b) Calculated results of the intensity distributions of the LCP SH waves in *k*-space at the real focal plane under RCP illumination. The four SH optical vortices channels, F_1, F_2, F_3, and F_4 were located at $(0, 0.083k_0)$, $(0, -0.083k_0)$, $(-0.083k_0, 0)$, and $(0.083k_0, 0)$, respectively. c) Measured results of the light intensity distributions of the LCP SH waves in *k*-space at the real focal plane under RCP illumination. d) Schematic of the block channels for LCP incidence. e) Calculated and f) measured results of the intensity distribution of the RCP SH waves at the virtual focal plane under LCP illumination.

SH radiation in the far field by using the Rayleigh–Sommerfeld diffraction integral[56]

$$U(x, y, z) = -\frac{i}{\lambda}\iint_S U(x_0, y_0) \times \frac{\exp(ikr)}{r} \times \cos(\vec{n}, \boldsymbol{r})\mathrm{d}S \tag{8}$$

where $U(x_0,y_0)$ is the complex amplitude profile in the metasurface plane ($z = 0$) with surface area S and normal direction $\vec{n}$, $\boldsymbol{r}$ is the vector between the point in the metasurface plane and a point in the focus plane ($z = f$), and $k = 2\pi/\lambda$ is the wavevector. Because the designed metasurface generates only SHG with opposite spin to the illumination light, the numerical intensity distribution of LCP in *k*-space at the focal plane ($z = 300$ μm) is depicted in Figure 3b. Figure 3c shows the measured intensity distributions at the focal plane, which is consistent with the numerical intensity distribution. Since the amplitude scale factor a_k is the same for each channel, the optical vortex (F_1) with topological charges $l_1 = +1$ has the strongest light intensity of SH and the smallest diameter of the annular ring, while the optical vortex (F_2) with topological charges $l_2 = +3$ has the weakest light intensity of SH and the largest diameter. Conventionally, by controlling the polarization of the incident light, the dual-polarity plasmonic phase-only metalens based on P–B phase can generate the real focal point at the real focal plane and the virtual focal point at the virtual focal plane, respectively. It means that the optical functionalities of the geometric phase-only multiplexing metasurfaces are conjugate for RCP and LCP illuminations (see Figure S4 in the Supporting Information). On the contrary, our nonlinear device breaks the conjugate symmetry, and the multichannels are blocked when the device is illuminated by LCP waves (Figure 3d). Since the nonlinear P–B phase still plays an important role in our design, as shown in numerical results (Figure 3e), the focused energy of SH waves is still generated at the designed position at the virtual focal plane ($z = -300$ μm). Obviously, the energy of blocked channels at the virtual plane is much weaker than the energy of the optical vortex channels at the real focal plane. The intensity distribution at the focal plane was also experimentally measured, as shown in Figure 3f, which is in good agreement with the numerical results. In particular, several new focuses were generated at the specific positions except for the original focuses. Under the group effect, the blocked channels are due to negative interference and the new focuses are due to positive interference. By comparing the optical vortices channels at the real focal plane and block channels at the virtual focal plane, we can demonstrate the excellent performance of the designed metasurface and the validity of our design strategy. Besides, we designed the second sample with four channels under LCP illumination (see Figure S5 in the Supporting Information). Compared with the first sample, the channel behaviors of the second sample for RCP and LCP illuminations are exchanged. As the manipulation of the full complex-amplitude modulation of SH waves, the proposed nonlinear metasurfaces can realize the spin-selective SHG optical vortices with independent topological charges, which further verifies our theory.

The aforementioned nonlinear metasurface can only achieve transmitted information for the incident light with specific circular polarization. Increasing the degree of freedom of spin

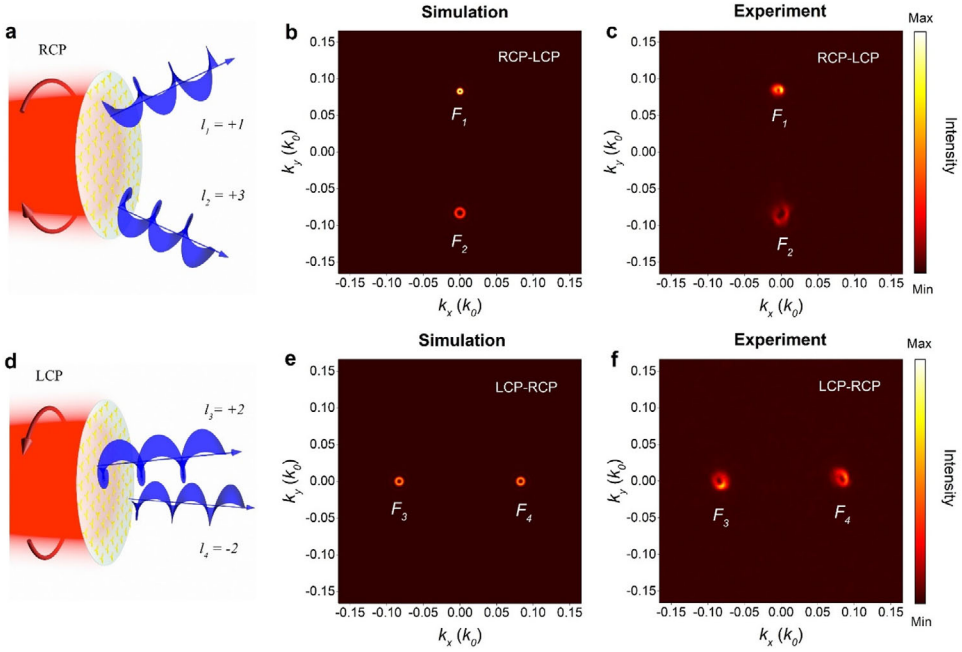

Figure 4. Observation of different series of multichannel vortex beams with spin-controlled multifunctional nonlinear metasurfaces. Schematic of the multichannel vortex beams with designed metasurface for a) RCP and d) LCP incidences. Calculated b) LCP and e) RCP light intensity distributions of SH waves in *k*-space at the real focal plane for RCP and LCP incidences, respectively. The SH optical vortices channels F_1 and F_2 are located at $(0, 0.083k_0)$ and $(0, -0.083k_0)$ for RCP incidence, and F_3 and F_4 are located at $(-0.083k_0, 0)$ and $(0.083k_0, 0)$ for LCP incidence. Measured c) LCP and f) RCP light intensity distributions of SH waves in *k*-space at the real focal plane for RCP and LCP incidences, respectively.

angular momentum is deeply required to boost the development of multifunctional integrated optical devices. We also designed a spin-controlled multifunctional nonlinear metasurface consisting of complex unit cells. The complex unit cell is composed of two types of nanoparticles for RCP and LCP incident light, respectively. Using Equations (5)–(7), we can independently design the different series of multichannel vortex beams for different circularly polarized incident lights (see Figure S6 in the Supporting Information). As shown in **Figure 4**a,d, by changing RCP and LCP incident lights, the designed metasurfaces can realize different series of multichannel vortex beams. We numerically calculated the intensity distributions at the real focal plane for RCP and LCP incidences (Figure 4b,e). The proposed metasurfaces can generate focusing optical vortices channels F_1 and F_2 with topological charges $l_1 = +1$ and $l_2 = +3$ for RCP incidence, while generate channels F_3 and F_4 with topological charges $l_3 = +2$ and $l_4 = -2$ for LCP incidence. Note that the crosstalk effect between different series of channels is minimized because another set of channels diverges in the transmission direction. Therefore, we can successfully measure one set of channels at the focal plane. The measurement results are in agreement with the numerical ones, as shown in Figure 4c,f. The visible differences between the calculated and measured results in Figures 3 and 4 are mainly attributed to the structural differences due to fabricational tolerances, that also cause a slight redshift of the measured resonance wavelength (shown in Figure 1b). Since the complex-amplitude modulation is implemented by manipulating the resonance of the C_3-symmetric nanoparticles, the shift of the resonance wavelength shows a significant impact on the measurement results of the intensity distributions at the focal plane.

3. Conclusions and Outlook

In conclusion, we proposed and experimentally demonstrated the full complex-amplitude modulation of SH waves based on nonlinear metasurface. By utilizing the hydrodynamic model, we studied the SHG process of the designed nanoparticles. Our presented strategy has been well demonstrated by the designed metasurfaces which can generate spin-selective multichannel vortex beams. Besides, different series of multichannel vortex beams have been observed at the real focal plane by the designed spin-controlled multifunctional metasurfaces. Compared with traditional phase-modulated nonlinear metasurfaces, the proposed metasurfaces can increase the manipulating dimension and show unique capacity in the manipulation of SH waves. The proposed design strategy paves the way for the accurate complex-amplitude modulation of the SH waves. One key application of our design is nonlinear holography since the quality of the holographic image can be significantly improved by amplitude-phase holography.[57] Our approach can also be further extended to achieve high-quality hologram and high-capacity information communications.

4. Experimental Section

Sample Fabrication: The samples were prepared using standard electron beam lithography and lift-off process. First, the fused silica substrate was spun coated with a layer of poly(methyl methacrylate; PMMA) with a thickness of 120 nm. Then, a layer of poly(3,4-ethylenedioxythiophene) polystyrene sulfonate (PEDOT:PSS) with a thickness of 35 nm was spun-coated. The PEDOT:PSS layer was intended for charge release during the

EBL process which employed a 100 kV voltage, 200 pA current, and 1000 μC cm^{-2} dose. After defining the nanometer scale metasurface patterns by the EBL process, the PEDOT:PSS layer was removed with pure water for 60 s and the PMMA was developed with methyl isobutyl ketone/isopropyl alcohol (3:1) for 40 s. After that, a Cr layer (2 nm) and an Au layer (30 nm) were deposited on the resist by sequence utilizing electron beam evaporation deposition. During the final lift-off procedure, the Cr film was stripped by removing PMMA with hot acetone at a temperature of 60 °C for 20 min, remaining C_3-symmetric nanoparticles arrays on the substrate.

Experimental Procedure: An erbium-doped ultrafast fiber laser (Toptica Photonics AG FemtoFiber Pro NIR, repetition frequency: 80 MHz, pulse length: ≈80 fs) centered at 1550 nm was used as a fundamental beam source. The linear and nonlinear signals were measured by coupling the beam source to a home-built microscope. The polarizer (LP_1) and quarter-wave plate (QWP_1) were combined to generate the incident circularly polarized light. The metasurface was illuminated at normal incidence and the generated nonlinear optical vortices were filtered by another set of QWP_2 and LP_2, then collected with an objective, a tube lens, and a scientific camera. The objective, tube lens (Thorlabs ITL200), and camera were all integrated on a three-axis motorized translation stage to measure the multichannel optical vortices. For nonlinear measurement, the fundamental pulses had an average power of 350 mW and were focused to a spot with a diameter of ≈200 μm (by a lens with focal length of 150 mm), which corresponded to a peak intensity of 0.17 GW cm^{-2}. The SHG signals were captured by a 20× objective (SIGMA-KOKI PAL-20-NIR-HR-LC00 20 × numerical aperture = 0.45) and a sCMOS (Scientific complementary metal oxide semiconductor) camera (HAMAMATSU ORCA-Flash4.0 V3).

Supporting Information

Supporting Information is available from the Wiley Online Library or from the author.

Acknowledgements

Z.H., W.L., and Z.L. contributed equally to this work. This work was supported by the National Key Research and Development Program of China (Grant Nos. 2017YFA0303800 and 2016YFA0301102), the National Natural Science Fund for Distinguished Young Scholar (Grant No. 11925403), the National Natural Science Foundation of China (Grant Nos. 11974193, 11904181, 11904183, 91856101, and 11774186), the Natural Science Foundation of Tianjin for Distinguished Young Scientists (Grant No. 18JCJQJC45700), the China Postdoctoral Science Foundation (Grant Nos. 2018M640224 and 2021M690084), and the Royal Society International Exchanges (Grant No. IES\R3\193046).

Conflict of Interest

The authors declare no conflict of interest.

Data Availability Statement

The data that support the findings of this study are available from the corresponding author upon reasonable request.

Keywords

full complex-amplitude modulation, metasurfaces, nonlinear optics, second harmonic

Received: April 18, 2021
Revised: August 28, 2021
Published online:

[1] N. Yu, P. Genevet, M. A. Kats, F. Aieta, J. P. Tetienne, F. Capasso, Z. Gaburro, *Science* **2011**, *334*, 333.
[2] X. Ni, N. K. Emani, A. V. Kildishev, A. Boltasseva, V. M. Shalaev, *Science* **2012**, *335*, 427.
[3] Z. Li, W. Liu, H. Cheng, S. Chen, *Sci. China: Phys. Mech. Astron.* **2020**, *63*, 284202.
[4] N. Yu, F. Capasso, *Nat. Mater.* **2014**, *13*, 139.
[5] P. Genevet, F. Capasso, F. Aieta, M. Khorasaninejad, R. Devlin, *Optica* **2017**, *4*, 139.
[6] P. Yu, J. Li, C. Tang, H. Cheng, Z. Liu, Z. Li, Z. Liu, C. Gu, J. Li, S. Chen, J. Tian, *Light: Sci. Appl.* **2016**, *5*, e16096.
[7] W. Liu, S. Chen, Z. Li, H. Cheng, P. Yu, J. Li, J. Tian, *Opt. Lett.* **2015**, *40*, 3185.
[8] P. Georgi, C. Schlickriede, G. Li, S. Zhang, T. Zentgraf, *Optica* **2017**, *4*, 1000.
[9] R. C. Devlin, A. Ambrosio, N. A. Rubin, J. P. B. Mueller, F. Capasso, *Science* **2017**, *358*, 896.
[10] J. Han, Y. Intaravanne, A. Ma, R. Wang, S. Li, Z. Li, S. Chen, J. Li, X. Chen, *Laser Photonics Rev.* **2020**, *14*, 2000146.
[11] L. Yu, Y. Fan, Y. Wang, C. Zhang, W. Yang, Q. Song, S. Xiao, *Laser Photonics Rev.* **2020**, *14*, 1900324.
[12] C. Hao, S. Gao, Q. Ruan, Y. Feng, Y. Li, J. K. Yang, Z. Li, C. W. Qiu, *Laser Photonics Rev.* **2020**, *14*, 2000017.
[13] F. Zhao, R. Lu, X. Chen, C. Jin, S. Chen, Z. Shen, C. Zhang, Y. Yang, *Laser Photonics Rev.* **2021**, *15*, 2100097.
[14] Z. Li, W. Liu, H. Cheng, J. Liu, S. Chen, J. Tian, *Sci. Rep.* **2016**, *6*, 35485.
[15] F. Aieta, P. Genevet, N. Yu, M. A. Kats, Z. Gaburro, F. Capasso, *Nano Lett.* **2012**, *12*, 1702.
[16] C. Wang, W. Liu, Z. Li, H. Cheng, Z. Li, S. Chen, J. Tian, *Adv. Opt. Mater.* **2018**, *6*, 1701047.
[17] X. Ling, X. Zhou, X. Yi, W. Shu, Y. Liu, S. Chen, H. Luo, S. Wen, D. Fan, *Light: Sci. Appl.* **2015**, *4*, e290.
[18] Z. Li, W. Liu, H. Cheng, S. Chen, J. Tian, *Adv. Opt. Mater.* **2017**, *5*, 1700413.
[19] F. Zhang, M. Pu, X. Li, P. Gao, X. Ma, J. Luo, H. Yu, X. Luo, *Adv. Funct. Mater.* **2017**, *27*, 1704295.
[20] N. Shitrit, J. Kim, D. S. Barth, H. Ramezani, Y. Wang, X. Zhang, *Phys. Rev. Lett.* **2018**, *121*, 046101.
[21] X. Chen, L. Huang, H. Muhlenbernd, G. Li, B. Bai, Q. Tan, G. Jin, C. W. Qiu, S. Zhang, T. Zentgraf, *Nat. Commun.* **2012**, *3*, 1198.
[22] L. Huang, X. Chen, H. Muhlenbernd, G. Li, B. Bai, Q. Tan, G. Jin, T. Zentgraf, S. Zhang, *Nano Lett.* **2012**, *12*, 5750.
[23] S. Chen, Y. Cai, G. Li, S. Zhang, K. W. Cheah, *Laser Photonics Rev.* **2016**, *10*, 322.
[24] F. Aieta, P. Genevet, M. A. Kats, N. Yu, R. Blanchard, Z. Gaburro, F. Capasso, *Nano Lett.* **2012**, *12*, 4932.
[25] S. Chen, Z. Li, Y. Zhang, H. Cheng, J. Tian, *Adv. Opt. Mater.* **2018**, *6*, 1800104.
[26] J. Jin, M. Pu, Y. Wang, X. Li, X. Ma, J. Luo, Z. Zhao, P. Gao, X. Luo, *Adv. Mater. Technol.* **2017**, *2*, 1600201.
[27] Z. Li, H. Cheng, Z. Liu, S. Chen, J. Tian, *Adv. Opt. Mater.* **2016**, *4*, 1230.
[28] L. Liu, X. Zhang, M. Kenney, X. Su, N. Xu, C. Ouyang, Y. Shi, J. Han, W. Zhang, S. Zhang, *Adv. Mater.* **2014**, *26*, 5031.
[29] M. Kim, A. M. H. Wong, G. V. Eleftheriades, *Phys. Rev. X* **2014**, *4*, 041042.
[30] W. Liu, Z. Li, Z. Li, H. Cheng, C. Tang, J. Li, S. Chen, J. Tian, *Adv. Mater.* **2019**, *31*, 1901729.
[31] B. Sain, C. Meier, T. Zentgraf, *Adv. Photonics* **2019**, *1*, 024002.
[32] S. Rubin, Y. Fainman, *Adv. Photonics* **2019**, *1*, 066003.
[33] A. P. Anthur, H. Zhang, R. Paniagua-Dominguez, D. A. Kalashnikov, S. T. Ha, T. W. Maß, A. I. Kuznetsov, L. Krivitsky, *Nano Lett.* **2020**, *20*, 8745.

[34] A. Fedotova, M. Younesi, J. Sautter, A. Vaskin, F. J. Löchner, M. Steinert, R. Geiss, T. Pertsch, I. Staude, F. Setzpfandt, *Nano Lett.* **2020**, *20*, 8608.
[35] Y. Tang, Z. Liu, J. Deng, K. Li, J. Li, G. Li, *Laser Photonics Rev.* **2020**, *14*, 2000085.
[36] J. Chen, K. Wang, H. Long, X. Han, H. Hu, W. Liu, B. Wang, P. Lu, *Nano Lett.* **2018**, *18*, 1344.
[37] C. Schlickriede, N. Waterman, B. Reineke, P. Georgi, G. Li, S. Zhang, T. Zentgraf, *Adv. Mater.* **2018**, *30*, 1703843.
[38] C. Schlickriede, S. S. Kruk, L. Wang, B. Sain, Y. Kivshar, T. Zentgraf, *Nano Lett.* **2020**, *20*, 4370.
[39] W. Ye, F. Zeuner, X. Li, B. Reineke, S. He, C. W. Qiu, J. Liu, Y. Wang, S. Zhang, T. Zentgraf, *Nat. Commun.* **2016**, *7*, 11930.
[40] E. Almeida, O. Bitton, Y. Prior, *Nat. Commun.* **2016**, *7*, 12533.
[41] D. Frese, Q. Wei, Y. Wang, M. Cinchetti, L. Huang, T. Zentgraf, *ACS Photonics* **2021**, *8*, 1013.
[42] G. Li, L. Wu, K. F. Li, S. Chen, C. Schlickriede, Z. Xu, S. Huang, W. Li, Y. Liu, E. Y. B. Pun, T. Zentgraf, K. W. Cheah, Y. Luo, S. Zhang, *Nano Lett.* **2017**, *17*, 7974.
[43] Z. Li, W. Liu, Z. Li, C. Tang, H. Cheng, J. Li, X. Chen, S. Chen, J. Tian, *Laser Photonics Rev.* **2018**, *12*, 1800164.
[44] M. Ma, Z. Li, W. Liu, C. Tang, Z. Li, H. Cheng, J. Li, S. Chen, J. Tian, *Laser Photonics Rev.* **2019**, *13*, 1900045.
[45] F. Walter, G. Li, C. Meier, S. Zhang, T. Zentgraf, *Nano Lett.* **2017**, *17*, 3171.
[46] G. Li, S. Chen, N. Pholchai, B. Reineke, P. W. Wong, E. Y. Pun, K. W. Cheah, T. Zentgraf, S. Zhang, *Nat. Mater.* **2015**, *14*, 607.
[47] M. Tymchenko, J. S. Gomez-Diaz, J. Lee, N. Nookala, M. A. Belkin, A. Alu, *Phys. Rev. Lett.* **2015**, *115*, 207403.
[48] D. Kim, J. Yu, I. Hwang, S. Park, F. Demmerle, G. Boehm, M.-C. Amann, J. Lee, *Nano Lett.* **2020**, *20*, 8032.
[49] N. Mao, J. Deng, X. Zhang, Y. Tang, M. Jin, Y. Li, X. Liu, K. Li, T. Cao, K. Cheah, H. Wang, J. Ng, G. Li, *Nano Lett.* **2020**, *20*, 7463.
[50] Z. Li, W. Liu, G. Geng, Z. Li, J. Li, H. Cheng, S. Chen, J. Tian, *Adv. Funct. Mater.* **2020**, *30*, 1910744.
[51] C. Ciracì, E. Poutrina, M. Scalora, D. R. Smith, *Phys. Rev. B* **2012**, *85*, 201403.
[52] K. Konishi, T. Higuchi, J. Li, J. Larsson, S. Ishii, M. Kuwata-Gonokami, *Phys. Rev. Lett.* **2014**, *112*, 135502.
[53] S. Chen, G. Li, F. Zeuner, W. H. Wong, E. Y. Pun, T. Zentgraf, K. W. Cheah, S. Zhang, *Phys. Rev. Lett.* **2014**, *113*, 033901.
[54] E. D. Palik, *Handbook of Optical Constants of Solids*, Academic Press, New York **1998**.
[55] N. Segal, S. Keren-Zur, N. Hendler, T. Ellenbogen, *Nat. Photonics* **2015**, *9*, 180.
[56] Y. Hu, Z. Wang, X. Wang, S. Ji, C. Zhang, J. Li, W. Zhu, D. Wu, J. Chu, *Light: Sci. Appl.* **2020**, *9*, 119.
[57] A. C. Overvig, S. Shrestha, S. C. Malek, M. Lu, A. Stein, C. Zheng, N. Yu, *Light: Sci. Appl.* **2019**, *8*, 92.